Exposed water ice on the nucleus of comet

67P/Churyumov-Gerasimenko

Authors: G. Filacchione[1*], M. C. De Sanctis[1], F. Capaccioni[1], A. Raponi[1], F. Tosi[1], M. Ciarniello[1], P. Cerroni[1], G. Piccioni[1], M. T. Capria[1], E. Palomba[1], G. Bellucci[1], S. Erard[2], D. Bockelee-Morvan[2], C. Leyrat[2], G. Arnold[3], M. A. Barucci[2], M. Fulchignoni[2], B. Schmitt[4], E. Quirico[4], R. Jaumann[3], K. Stephan[3], A. Longobardo[1], V. Mennella[5], A. Migliorini[1], E. Ammannito[6], J. Benkhoff[7], J. P. Bibring[8], A. Blanco[9], M. I. Blecka[10], R. Carlson[11], U. Carsenty[3], L. Colangeli[7], M. Combes[2], M. Combi[12], J. Crovisier[2], P. Drossart[2], T. Encrenaz[2], C. Federico[13], U. Fink[14], S. Fonti[9], W. H. Ip[15], P. Irwin[16], E. Kuehrt[3], Y. Langevin[8], G. Magni[1], T. McCord[17], L. Moroz[3], S. Mottola[3], V. Orofino[9], U. Schade[18], F. Taylor[16], D. Tiphene[2], G. P. Tozzi[19], P. Beck[4], N. Biver[2], L. Bonal[4], J-Ph. Combe[17], D. Despan[2], E. Flamini[20], M. Formisano[1], S. Fornasier[2], A. Frigeri[1], D. Grassi[1], M. S. Gudipati[11], D. Kappel[3], F. Mancarella[9], K. Markus[3], F. Merlin[2], R. Orosei[21], G. Rinaldi[1], M. Cartacci[1], A. Cicchetti[1], S. Giuppi[1], Y. Hello[2], F. Henry[2], S. Jacquinod[2], J. M. Reess[2], R. Noschese[1], R. Politi[1], G. Peter[22]

Affiliations:

[1]INAF-IAPS, Istituto di Astrofisica e Planetologia Spaziali, Rome Italy

[2]LESIA, Observatoire de Paris/CNRS/UPMC/Université Paris-Diderot, Meudon, France

[3]Institute for Planetary Research, DLR, Berlin, Germany

[4]Univ. Grenoble Alpes, CNRS, IPAG, Grenoble, France

[5]INAF-Osservatorio di Capodimonte, Napoli, Italy

[6]UCLA, Los Angeles, USA

[7]European Space Agency – ESTEC, The Netherlands

[8]Institut d'Astrophysique Spatial CNRS, Orsay, France

[9]Dipartimento di Matematica e Fisica "Ennio De Giorgi", Università del Salento, Italy

[10]Space Research Centre, Polish Academy of Sciences, Warsaw, Poland

[11]NASA JPL, Pasadena, USA

[12]Space Physics Research Laboratory, The University of Michigan, Ann Arbor, USA

[13]Università di Perugia, Italy

[14]Lunar Planetary Laboratory, University of Arizona, Tucson, USA

[15]National Central University, Taipei, Taiwan

[16]Departement of Physics, Oxford University, Oxford, UK

[17]Bear Fight Institute, Winthrop, WA, USA

[18]Helmholtz-Zentrum Berlin für Materialien und Energie, Germany

[19]INAF-Osservatorio Astrofisico di Arcetri, Firenze, Italy

[20]Agenzia Spaziale Italiana, Rome, Italy

[21]Istituto di Radioastronomia – INAF, Bologna, Italy

[22]Institute of Optical Sensor Systems, DLR, Berlin, Germany

*Correspondence to: gianrico.filacchione@iaps.inaf.it, phone +39-0645488454

Abstract: **Although water vapour is the main gaseous species observed in 67P/Churyumov-Gerasimenko's (67P/CG) coma [1, 2] and water is the major constituent of cometary nuclei [3, 4], limited evidences for exposed water ice regions on the nucleus' surface has been found so far [5, 6]. The nucleus appears mainly to be uniformly coated by dark, dehydrated, refractory and organic-rich material [7]. The absence of large regions of exposed water ice seems a common finding on the surfaces of many of the comets observed so far [8, 9, 10].**

Here we report the identification at infrared wavelengths of water ice on two debris falls in the Imhotep region of the nucleus in which it has been exposed on the walls of elevated structures and at the base of the wall. A quantitative derivation of the water ice abundance in these regions indicates the presence of millimetre-sized pure ice grains, considerably larger than in all previous observations [6, 8, 9, 10]

While micron-sized water ice grains are the usual result of vapour recondensation in ice free layers [6], the occurrence of millimetre-sized grains of pure ice as observed in the Imhotep debris falls is best explained by grain growth of ice particles by vapour diffusion in ice-rich layers, or by sintering. As a consequence of these processes, the nucleus can

develop an extended and complex layering in which the outer dehydrated crust [7] is superimposed on water ice enriched layers. The stratigraphy observed on 67P/CG [11, 12] is the result of evolutionary processes affecting the uppermost metres of the nucleus and does not necessarily require a global layering to have occurred at the time of formation of the comet.

Located in the bottom part of 67P/CG main lobe, the Imhotep plain is characterized by a 1 km x 1.5 km wide smooth terrain unit filled by very fine dust *[11, 13]*. The region is circumscribed by elevated structures, some of them showing circular shape with well-defined walls, which display erosion and mass wasting on their sides *[14]*. Rosetta's navigation cameras identified bright albedo patches (BAP) on the walls of two of these features (*Fig. 1*): a flat-floored raised circular structure with an external rim partially collapsed located at the Ash-Khepry-Imhotep boundary at lon. 117°E, lat. 13°N (BAP#1) and a hill with a steep slope at lon. 180°-182°E, lat. 4°-10°S (BAP#2). Both areas are exposed towards the lower Imhotep plain where the waste material is accumulated as boulders and debris at the bottom of the cliffs. These deposits are located on relatively cold, collapsed walls of elevated structures and seem to be recently exposed. The debris falls indicate material eroded and deposited at the base of walls. The overall geological context points to a process in which limited amounts of bedrock material break out of the wall and distribute as disrupted fragments at the bottom of the affected wall regions. Mechanisms that can trigger the falls are related to water ice sublimation, water ice metamorphism, thermal cracking or possibly impacts.

The best views of the two BAPs obtained by the Visual InfraRed Thermal Imaging Spectrometer VIRTIS-M *[15]* are shown in *Fig. 2*. The description of these observations, including the retrieval of the spectral parameters and the associated temperature maps, are discussed in the *Methods* section.

In the two BAP regions, VIRTIS-M has detected prominent absorption features at 1.05, 1.25, 1.5 (partial), and 2.0 µm (discussed later in *Fig. 3*). These spectral features represent a clear evidence of the presence of water ice. When observing the water ice rich areas the 3.2 µm band, ubiquitously observed throughout the cometary nucleus and interpreted *[7]* as caused by the

presence of organic compounds, appears deformed by the strong 3.0 µm signature of water ice. This is the case of the Hapi active region, where it appears in form of transient deposits formed in the upper layer of the surface by recondensation of water molecules sublimated from sub-surface ice during the diurnal cycle *[6]*.

With the aim of verifying the spectral properties of the observed water ice regions and to study their persistence during the first few months of the mission, we have performed a temporal analysis of the 2 µm band appearance while we use the entire 1-4 µm spectral range to quantitatively derive the water ice abundance and grain size. In *Fig. 3* we show the 2 µm band depth time series (see *Methods* section for analysis details) for a BAP#1 neighbourhood using all the spectra measured in the period 23th September - 21th November 2014 (*Fig. 3a-3b*) and for BAP#2 obtained between 2nd and 23th September 2014 (*Fig. 3c*). The persistence of the 2 µm band absorption is evident during these time periods, resulting in average values of 5.6-7.6% for BAP#1 and 5.0% for BAP#2.

The spectral analyses show no significant change of the bands centres and depths during the period of observation, indicating that the ice is stable over that timeframe. After linear spectral continuum removal, the 2.0 µm band centre appears located at 2.04 µm for BAP#1 (*Fig. 3d*), with an average band depth of 5%. A band centre located at wavelengths slightly longer than 2.0 µm is diagnostic of crystalline water ice, as opposed to the amorphous phase which has the band centre located at 2.0 µm *[16]*. A secondary minimum of the 1.5 µm band, located at about 1.65 µm is typical feature of water ice in the crystalline form while it is absent in amorphous ice *[17];* in *Fig. 3e* VIRTIS-M data partially show the long wavelength wing of the 1.5 µm band where the secondary minimum at about 1.65 µm is clearly seen. Finally, in few well-resolved pixels the weaker 1.05 and 1.25 µm bands of water ice have been also identified. (*Fig. 3e*).

VIRTIS-M reflectance spectra were modelled following the approach described in the *Methods* section. The best-fitting result shown in *Fig. 4a*, for a representative spectrum of BAP#1, corresponds to an areal mixing in which 1.2% of the pixel area is occupied by patches of large grains of diameter around 2 mm for this specific case of pure water ice while the remaining 98.8% of the pixel area is composed of an intimate mixture of water ice (3.4%, grains of 56 µm in diameter) and dark terrain (95.4%). As a result, the total amount of surface water ice on the simulated spectrum correspond to about 4.6% for a pixel sampling an area of about 2.5 m x 2.5

m. By repeating this fitting technique on each pixel of the two high-resolution images shown in *Fig. 2c-2e*, we have derived water ice abundance maps for the two debris falls in which intimate and areal mixing of ice coexist within the dark terrain (*Fig. 4b-4c-4d-4e*). The maximum water ice abundances, equivalent to about 1.2% and 4% for the areal and intimate cases respectively, correspond to those of the bluish waste material accumulated at the base of the two debris falls. A similar water ice abundance (6%) was observed by the Deep Impact mission on the 0.5 km^2 wide water ice deposits identified, by using a linear mixing technique, on the surface of 9P/Tempel 1 *[8]*.

The size range of ice grains that produces the best fits in the observed areas displays a clear bimodal distribution (*Extended Data Figure 1* of the *Methods* section), where 76% of the pixels in the intimate mixtures have grain sizes between 33-72 μm, and 68% of the pixels in the pure ice patches regions have grain sizes between 1.4-2.6 mm. In a previous paper *[6]*, we showed that the diurnal mechanism of ice trapping in the dehydrated uppermost layer led to the formation of ice grains of only few microns in diameter. Thus, the VIRTIS-M observations indicate the presence of three different populations of icy grains on the nucleus surface, which imply different growth mechanisms and different spatial and time scales for their occurrence.

Small water ice grains are the result of the fast condensation process occurring at each comet rotation on the Hapi area in the thin (cm-sized) uppermost ice-free layers *[6]*. This is consistent with Deep Impact observations of the size distribution of released ice grains immediately after the impact event *[18]*. On the other hand, the occurrence of mm-sized grains of 'pure' ice as observed over large areas (metre-sized) on the Imhotep debris falls, represents the occasional exposure of deeper layers which have been subjected to a more complex history. Assuming a size range of tens of micron as a typical size for ice grains present on the nucleus of comets *[8, 9, 10 and our results]*, the observations of mm-sized grains can be explained by the growth of secondary ice crystals from vapour diffusion in ice-rich colder layers and/or by ice grains sintering *[19, 20]*. The energy necessary to activate these processes is provided by the thermal heat wave penetrating into the subsurface layers and causing ice sublimation; the additional contribution to the total energy balance derived from the amorphous to crystalline phase transition should not be neglected although it is expected to represent a moderate contribution *[19]*. Ice grain growth can profoundly alter the thermal evolution of the nucleus as it causes a decrease in porosity (densification) and an increase in thermal conductivity. Models

show that the ice grain growth and the densification can encompass layers of several metres *[20]* thus affecting the large-scale structural and thermal properties of the nucleus. Moreover, the KOSI experimental results showed that, depending on the dust/ice ratio, more than 80% of the sublimating ice was not released through the dust mantle but re-deposited at greater depths *[21]*. As a consequence, the observed stratification, which is one of the most prominent structural features of 67P/CG *[11, 12]*, would be the result of cometary evolution processes rather than a remnant of the nucleus formation scenario.

References and Notes:

[1] M. Hässig et al., Time variability and heterogeneity in the coma of 67P/Churyumov-Gerasimenko, Science 347, (2015).

[2] S. Gulkis et al., Subsurface properties and early activity of comet 67P/Churyumov-Gerasimenko, Science 347, (2015).

[3] M. J. Mumma and S. B. Charnley, The Chemical Composition of Comets – Emerging Taxonomies and Natal Heritage, Annu. Rev. Astron. Astrophys. 49, 471–524, (2011).

[4] P. Ehrenfreund, S. B. Charnley, D. H. Wooden, From interstellar material to cometary particles and molecules, in Comets II, M. C. Festou, H. U. Keller, and H. A. Weaver (eds.), University of Arizona Press, Tucson, 745 pp., 115-133, (2004).

[5] A. Pommerol et al., OSIRIS observations of meter-size exposures of H_2O ice at the surface of 67P/Churyumov-Gerasimenko and interpretation using laboratory experiments, A&A, in press. DOI:10.1051/0004-6361/201525977

[6] M. C. De Sanctis, et al., The diurnal cycle of water ice on comet 67P/Churyumov-Gerasimenko, Nature, 525, 500-503 (2015).

[7] F. Capaccioni, et al., The organic-rich surface of comet 67P/Churyumov-Gerasimenko as

seen by VIRTIS/Rosetta, Science, 347, (2015).

[8] J. M. Sunshine et al., Exposed Water Ice Deposits on the Surface of Comet 9P/Tempel 1, Science, 311, 1453-1455, (2006).

[9] A'Hearn, M. F. et al., EPOXI at comet Hartley 2, Science, 332, 1396-1400, (2011).

[10] J.M. Sunshine et al.. The Distribution of Water Ice on Comet 103P/Hartley 2. LPI Contributions, vol. 1667, p. 6438, (2012)

[11] N. Thomas, et al., The morphological diversity of comet 67P/Churyumov-Gerasimenko, Science, 347, (2015).

[12] M. Massironi et al., The two independent and primitive envelopes of the bilobate nucleus of comet 67P, Nature, doi:10.1038/nature15511.

[13] H. Sierks et al., On the nucleus structure and activity of comet 67P/Churyumov-Gerasimenko, Science, 347, (2015).

[14] A. T. Auger et al., Geomorphology of the Imhotep region on comet 67P/Churyumov-Gerasimenko from OSIRIS observations, A&A, in press.

[15] A. Coradini et al., Virtis: An Imaging Spectrometer for the Rosetta Mission, Space Sci. Rev. 128, 529–559, (2007).

[16] W. M. Grundy, B. Schmitt, The temperature-dependent near-infrared absorption spectrum of hexagonal H_2O ice, JGR, 103, issue E11, 25809-25822, (1998).

[17] R. M. Mastrapa et al., Optical constants of amorphous and crystalline H_2O ice in the near infrared from 1.1 to 2.6 μm, Icarus, 197, 307-320, (2008).

[18] J. M. Sunshine et al., The distribution of water ice in the interior of Comet Tempel 1, Icarus, 190, 284-294, (2007).

[19] D. Prialnik, J. Benkhoff, M. Podolack, Modeling the structure and activity of comet nuclei, in Comets II, M. C. Festou, H. U. Keller, and H. A. Weaver (eds.), University of Arizona Press, Tucson, 115-133, (2004)

[20] K. J. Kossacki, S. L. Szutowicz, J. Leliwa-Kopystyński, Comet 46P/Wirtanen: Evolution of the Subsurface Layer, Icarus, 142, 202-218, (1999).

[21] J. Benkhoff, K. J. Seidensticker, K. Seiferlin, T. Spohn, Energy analysis of porous water ice under space-simulated conditions: results from the KOSI-8 experiment, Planet. Space Sci., 43, Nos. 314, 353-361, (1995).

made use of NASA's Astrophysics Data System. With fond memories of dr. Angioletta Coradini, conceiver of the VIRTIS instrument, our leader and friend.

Corresponding author information:

Gianrico Filacchione

INAF-IAPS, via del Fosso del Cavaliere, 100, 00133, Rome, ITALY

gianrico.filacchione@iaps.inaf.it

phone: +39-0645488454

Legends for main figures

Figure 1: Rosetta NAVCAM context images of the two debris falls. **Panel a)** Imhotep region showing BAP#1 on the Ash-Khepry-Imhotep boundary (white arrow) and BAP #2 on the hillside (yellow arrow). **Panel b)** waste material and debris accumulated at the bottom of the landslide eroding the side of the elevated circular structure. BAP #1 is not visible in the viewing geometry of this nadir pointing image. **Panel c)** BAP #1 bright albedo patch caused by the presence of water ice is clearly visible on this oblique view of the elevated structure wall. **Panel d)** Similar viewing geometry identifying BAP#2.

Figure 2: VIRTIS-M observations of the two water ice debris falls. **Panel a)** Colour image showing BAP#1-2 (white and yellow arrows, respectively). **Panel b)** Water ice-rich waste terrain on BAP#1 is visible in blue colour on the right side of the circular elevated structure. **Panel c)** Close-up acquisition on BAP#1 reveals the bluish colour of the water ice-rich unit. **Panel d)** Temperature map showing the water ice-rich terrain at T<160 K. **Panel e)** Hill side image showing BAP#2. **Panel f)** Temperature map showing the water ice rich terrain at T<180 K. All colour images are obtained from B=1.3 μm, G=2.0 μm, R=2.9 μm channels.

Figure 3: Spectral evidences of water ice. **Panels a-b)** 2 μm band depth time series for BAP#1 in October (MTP008) and November (MTP009) 2014. **Panel c)** same as panels a-b) but for BAP#2 on September (MTP007) 2014 dataset. Fluctuations are due to the varying signal to noise caused by the changing illumination and viewing conditions during the observations. **Panel d)** Median spectra derived from MTP008-009 datasets BAP#1 showing the 2 μm absorption feature. Continuum-removed (CR) data show the spectral position of the band centre at about 2.04 μm, compatible with water ice in crystalline form. The 2 μm feature is not evident on the BAP#2 median spectrum derived from the entire MTP007 dataset but it appears only on limited observations, like the SP2237 one, marked by a blue dash line in panel c). **Panel e)** Comparison of BAP #1 median spectrum where only the 1.65 and 2 μm bands are visible with a water ice-rich pixel (SP1446, indicated by the blue dash line in panel a) which clearly shows the 1.05, 1.25, 1.5-1.65 and 2.05 μm pure crystalline water ice absorption features. This spectrum can be simulated with two end members, e.g. crystalline water ice and dark terrain (DT), as shown in Fig. 4. Instrumental order sorting filter junction wavelengths are marked by grey box.

Figure 4: Water ice spectral analysis and spatial distribution. **Panel a)** BAP#1 water ice-rich VIRTIS spectrum (black curve with error bars in red; at each wavelength the error corresponds to the inverse of signal-to-noise ratio) and best-fit synthetic model (blue curve). The location of the VIRTIS spectrum corresponds to the pixel indicated by an arrow in panels b-c). Instrumental order sorting filters junctions wavelengths are marked by grey boxes. **Panels b-c)** Water ice abundance maps for BAP#1 on observation I1_00371998843 (Fig. 2 panel c) in areal (b) and

intimate (c) mixing with dark material, respectively. **Panels d-e)** Water ice abundance maps for BAP#2 on observation I1_00369369214 (Fig. 2 panel e) in areal (d) and intimate mixing (e) with dark material, respectively. Black pixels in panels b-e) correspond mainly to shadow areas whose spectra are excluded from the analysis because they have a median signal-to-noise ratio <30, and for which a satisfactory model fit was not obtained. Estimated relative error for retrieved parameters is 20%.

METHODS SECTION

VIRTIS-M (Visible and InfraRed Thermal Imaging Spectrometer, Mapping channel) is the VIS-IR hyperspectral channel *[15]* aboard Rosetta. The instrument performs 0.25-5.1 µm spectroscopy by using two separate detectors, a CCD for the 0.25-1 µm and a HgCdTe for the 1.0-5.1 µm ranges, respectively. The spectral sampling is equal to 1.8 and 9.7 nm/band for the two channels, respectively. Both spectral channels share the same telescope equipped with a scanning mirror to build hyperspectral cubes. The instrumental Field of View (FOV) is equal to 3.7° with an Instantaneous Field of View (IFOV) of 250 µrad. The slit aperture is therefore acquired by 256 spatial samples. The raw data are converted to I/F by applying the calibration pipeline *[22, 23, 24]* and the corrections derived from in-flight data *[25, 26]*.

OBSERVATION CAMPAIGNS: during the Philae pre-landing phase, four different nucleus mapping campaigns have been carried out by VIRTIS-M: the first in August 2014, during the MTP006 mission period, when the spacecraft was orbiting between 50-100 km distances from the nucleus with 25°-40° solar phase angle. In this period a large number of observations was executed at constant solar phase (about 30°) with spatial resolution of 12.5 to 25 m/pixel, including the observation shown in *Fig. 2a* in which both debris falls are shown. The second phase occurred in September 2014, during MTP007, when the spacecraft was at about 30 km distance with 60°-70° solar phase angle. During this campaign both debris falls were observed by VIRTIS-M in oblique view with a spatial resolution of about 7.5 m/pixel (*Fig. 2b-2e*). The third campaign (MTP008) was executed in October 2014 when the spacecraft orbited

along the nucleus' terminator in circular orbits at 20 and then 10 km distances, resulting in observations with a spatial resolution of 5 to 2.5 m/pixel taken at solar phase angle of 90°. During the 10 km orbit VIRTIS-M acquired the best view of the waste material at the bottom of the BAP#1 (see *Fig. 2c*). Finally, the last campaign was executed from end of October to mid November 2014 in preparation of Philae lander release when the spacecraft's trajectory was on elliptic orbits between 10 and 20 km distances with VIRTIS-M continuing to monitor the nucleus with spatial resolution between 2.5 and 5 m/pixel with solar phase angle between 70° to 100°. During this period the visibility of the BAP#1 continued to be good while BAP#2 was no longer visible.

To take into account the local irregular topography we have expanded the range of coordinates over which our spectral analysis is performed to lon. 114°-120°E, lat. 11°-15°N for BAP#1 and to lon. 178°-184°E, lat. 2°-12°S for BAP #2. Overall, the best viewing of the two BAPs occurs during off-nadir pointing sequences and during Rosetta's terminator orbits where the emission angle on the exposed walls is smaller. The analysis of VIRTIS geo-referenced images of these areas shows that a total of 7,495 and 7,204 VIRTIS pixels in dayside illumination conditions are located above BAP#1 and #2, respectively. The corresponding 2 μm water ice band depth above these points is shown in *Fig. 3a-b-c* for the different MTP intervals. Fluctuations are due to the variable water ice distribution above the local rough topography with different illumination and viewing geometry occurring during Rosetta's orbits around the comet.

THERMAL IMAGES for the two more resolved observations of the debris fall regions are shown in *Fig. 2d-2f* at the same scale of the corresponding images in reflectance. VIRTIS-M data are used to derive the surface temperature by modelling spectral radiance in the 4.5-5.1 μm range adopting a Bayesian approach *[27]*. The retrieved temperature of a given point of the nucleus' surface is a function of the local terrain properties (albedo, composition, grain size, roughness, thermal conductivity, volatiles sublimation) and illumination geometry (solar incidence angle, local solar time, time since last shadow occurred). As a consequence of the large obliquity of the spin axis with respect to the orbital plane, the southern hemisphere, where the Imhotep plain is located, is considerably less illuminated than the northern hemisphere until few months before perihelion passage (which occurred in August 2015). This affects the average

temperatures measured on this region which are much lower than the ones measured on the smaller nucleus lobe and in the north part of the larger one *[2, 28]*. On the Imhotep plain, the MIRO experiment has measured a maximum diurnal subsurface temperature of about 120 K with both millimetre and submillimetre channels *[2]* while modelling VIRTIS-M data a diurnal surface temperature of 180-190±15 K has been inferred *[28]*. Such thermal conditions are favourable for preserving water ice on the surface *[29]*. In addition, *Fig. 2d-2f* clearly shows that BAP#1 and #2 are on average cooler than nearby terrains. In the thermal image of BAP #1, VIRTIS-M has measured a temperature lower than 160±30 K on pixels where water ice features are more prominent. On BAP#2, the temperature is below 180±15 K. This means that in both regions the water ice is close to the sublimation regime *[29]*.

SPECTRAL MODELLING: A quantitative spectral analysis of the composition of BAP#1-#2 has been performed using Hapke's radiative transfer model *[30]* as described in *[31]*. The two regions have been modelled using a complex mixture of two spectral endmembers: crystalline water ice, simulated by using optical constants measured at T=160 K between 1 and 4 µm *[17, 33, 34, 35]*, and a "dark terrain" (DT) unit corresponding to the average spectrum of the comet's surface after the application of photometric correction *[32]*. Both endmember spectra are shown in *Fig. 3e* in the 1.0-2.3 µm spectral range. The analysis has been performed on spectra normalized at 2.3 µm in order to rule out uncertainties on the radiometric and photometric accuracy as well as errors on the local geometry information, due to unresolved shadows and roughness.

In Hapke's theory *[30]* the ratio of the bidirectional reflectance r(i, e, g, λ) of a semi-infinite medium taken at two wavelengths λ and λ_0 can be expressed as:

$$\frac{r(i,e,g,\lambda)}{r(i,e,g,\lambda_0)} = \frac{\frac{w(\lambda)K}{4\pi}\frac{\mu_{0e}}{\mu_{0e}+\mu_e}\left[B_{SH}(g)p(g,\lambda) + H(w(\lambda),\mu_{0e}/K)H(w(\lambda),\mu_e/K) - 1\right]S(i,e,g,\theta)B_{CB}(g,\lambda)}{\frac{w(\lambda_0)K}{4\pi}\frac{\mu_{0e}}{\mu_{0e}+\mu_e}\left[B_{SH}(g)p(g,\lambda_0) + H(w(\lambda_0),\mu_e/K)H(w(\lambda_0),\mu_e/K) - 1\right]S(i,e,g,\theta)B_{CB}(g,\lambda)} \quad 1.)$$

where *i, e, g* are the incidence, emission and phase angle, respectively; *w* is the single scattering albedo (SSA); *K* is the porosity of the medium; *p(g, λ)* is the single particle phase function; μ_{0e}, μ_e are the effective cosines of the incidence and emission angles, differing from the μ_0 and *µ* because of the effect of surface roughness; *H(w, μ_e/K)* the Chandrasekhar functions

describing the multiple scattering components; $B_{SH}(g)$ the shadow hiding opposition effect term; $B_{CB}(g, \lambda)$ the coherent back-scattering opposition effect; $S(i, e, g, \theta)$ the shadow function modelling large scale roughness and θ the average surface slope. As we are taking a ratio, all the terms that do not depend on wavelength will disappear in eq. 1). In particular, the porosity K and the roughness embedded in the $S(i, e, g, \theta)$ shadow function are removed. Moreover, during the VIRTIS-M observations described in this paper the solar phase was fixed at g=95°. As a consequence the shadow hiding effect is negligible and this implies posing the terms B_{SH} and B_{CB} equal to 1.

In summary eq. 1.) will be simplified as follows:

$$\frac{r(i,e,g,\lambda)}{r(i,e,g,\lambda_0)} = \frac{w(\lambda)}{w(\lambda_0)} \left[\frac{p(g,\lambda) + H(w(\lambda), \mu_{0e}/K)H(w(\lambda), \mu_e/K) - 1}{p(g,\lambda_0) + H(w(\lambda_0), \mu_{0e}/K)H(w(\lambda_0), \mu_e/K) - 1} \right] \quad 2.)$$

In addition, for the dark terrain component, which makes up the majority by far of the material present on the nucleus surface, the contribution of the porosity and of the roughness to the multiple scattering term is a second order effect. Thus we can assume $\mu_{0e}/K=\mu_0$.

Eq. 2 represents the formulation to be used to derive the normalised reflectance of a single material but it can be straightforwardly extended to the case of a linear combination of reflectances, maintaining the simplifications described above. In this relation the parameters to fit are: the phase function $p(g)$ and the single scattering albedo w, which can be modelled using the optical constants and the grain size. The phase function $p(g)$ derived by [32] is used in the spectral modelling.

We are dealing with two end-members and we have used areal and intimate mixing modalities in the simulations: in the areal mixing the surface is modelled as patches of pure water ice and dark terrain, with each photon scattered within one patch. In the intimate mixing model the particles of the two end-member materials are in contact with each other and both are involved in the scattering of a single photon. In intimate mixing the single scattering albedo of the mixture is the weighted average, through their abundance P, of the Dark Terrain (DT) and Water Ice (WI) single scattering albedos. Thus the $w(\lambda)$ is given by $w(\lambda)=w(\lambda)_{DT} P_{DT} + w(\lambda)_{WI} P_{WI}$. In the areal mixing (linear mixing) instead, the two components are treated independently. For the dark terrain we have used the $w(\lambda)$ value retrieved from the photometric correction [32], while to

describe the water ice contribution we explicitly calculated the $w(\lambda)$ from the optical constants and from the grain size, which represent the parameter to be fitted. Furthermore, after extensive tests, we have been able to fix the value of the phase function p(g=95°)=0.5. With the approach described above the model's free-parameters are the percentage and grain size of the water ice in the intimate mixed phase, and the percentage and grain size of the water ice in the areal mixed phase.

Before fitting, the observed spectra are corrected for spikes, out of statistics signals and for instrumental artifacts. The best-fitting result, an example of which is shown in *Fig. 4a,* is obtained by applying the Levenberg-Marquardt method for nonlinear least squares multiple regression. In this specific case, the best matching spectrum corresponds to an areal mixing where 1.2% of the pixel area is modelled with large grains (size distribution peaked around 2 mm in diameter) of pure water ice while the remaining 98.8% of the pixel area is composed of an intimate mixture with 3.4% of water ice (size distribution peaked at 56 µm in diameter) with the remaining 95.4% of dark material. The distribution of the areal and intimate grain sizes appears to be monodispersed (*Extended Data Figure 1*) and grouped in two very different families: small grains of 50-60 µm diameter size in the intimate case and large mm-size grains in the areal case. When we say that our fit requires particles of average sizes of 2 mm, this means that, from a photon point of view, the medium is essentially continuous at scales of 2 mm. This implies that any discontinuities (e.g., voids) within a volume of 2 mm radius should be smaller than the wavelength.

NAVCAM IMAGES REFERENCES Rosetta NAVCAM context images of the two debris fall shown in Figure 1 are:

- ROS_CAM1_20140823T184003, taken on 2014-08-23T18:40 from a distance of 64.8 km (panel a). The BAP#1 on the Ash-Khepry-Imhotep boundary at lon. 117°E, lat. 13°N is indicated by the white arrow. The BAP #2 on the hillside placed at lon. 180°-182°E, lat. 4°-10°S is indicated by the yellow arrow;

- ROS_CAM1_20140914T121933 , taken on 2014-09-14T12:19 from a distance of 30.7 km (panel b). The image shows the waste material and debris accumulated at the bottom of the

landslide eroding the side of the elevated circular structure. BAP #1 is not visible in the viewing geometry of this nadir pointing image;

- ROS_CAM1_20140914T141723, taken on 2014-09-14T18:40 from a distance of 30.6 km (panel c). BAP #1 bright albedo patch caused by the presence of water ice is clearly visible on the oblique view of the elevated structure wall;

- ROS_CAM1_20140915T021834, taken on 2014-09-15T02:18 from a distance of 29.9 km (panel d). This image shows a viewing geometry identifying BAP#2 similar to panel c. Note a secondary smaller bright layer on the right of the primary.

VIRTIS-M HYPERSPECTRAL CUBES REFERENCES Rosetta VIRTIS-M observations of the two BAP shown in Figure 2 are the following:

- I1_00367585390, taken on 2014-08-25T11:04 with an integration time of 3 sec and a spatial resolution of 12.5 m/pixel (panel a);

- I1_00369364114, taken on 2014-09-15T01:09 with an integration time of 3 sec/line and a spatial resolution of 7.5 m/pixel (panel b);

- I1_00371998843, taken on 2014-10-15T13:01 with an integration time of 3 sec/line and a spatial resolution of 2.5 m/pixel (panels c-d);

- I1_00369369214, taken on 2014-09-15T02:34 with an integration time of 3 sec/line and a spatial resolution of 7.5 m/pixel (panels e-f).
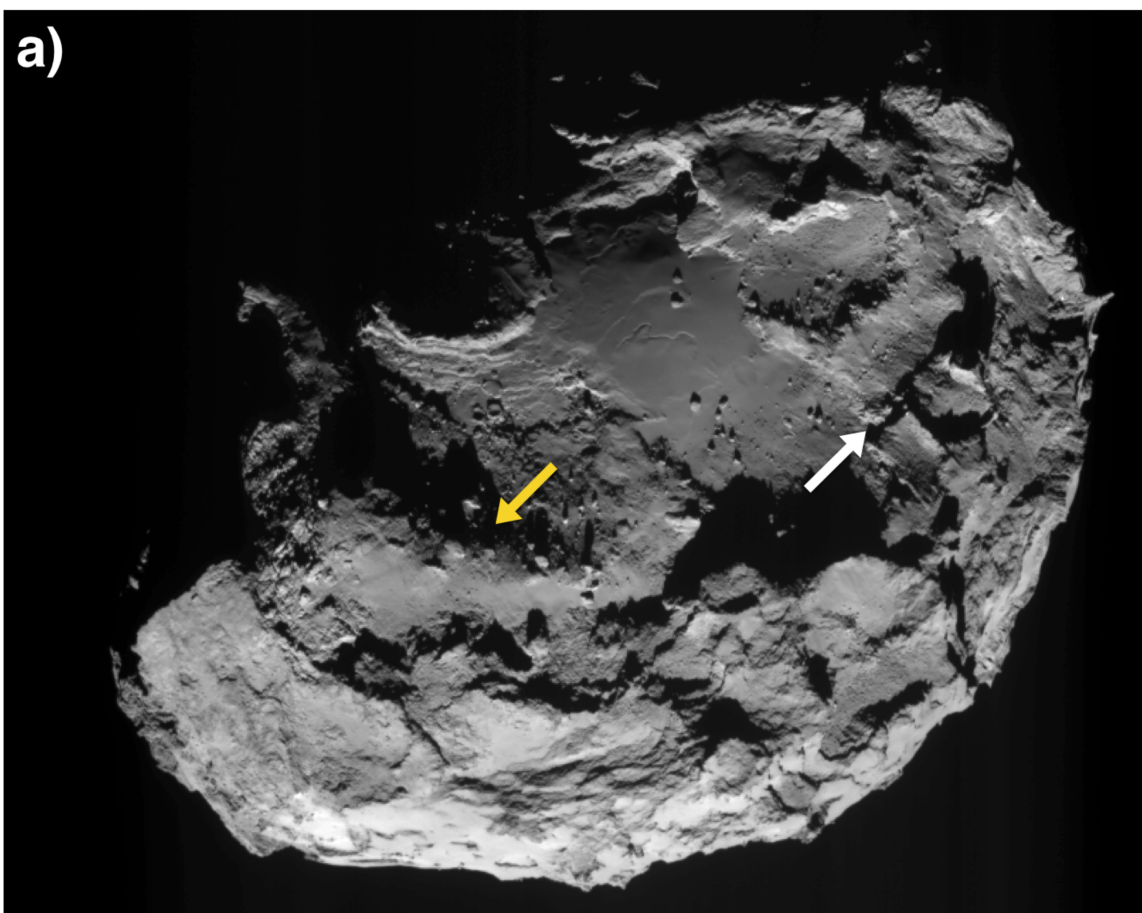
METHODS REFERENCES

[22] Filacchione, G., Calibrazioni a terra e prestazioni in volo di spettrometri ad immagine nel visibile e nel vicino infrarosso per l'esplorazione planetaria, PhD dissertation, Università degli Studi di Napoli Federico II, 316 pages, (2006).
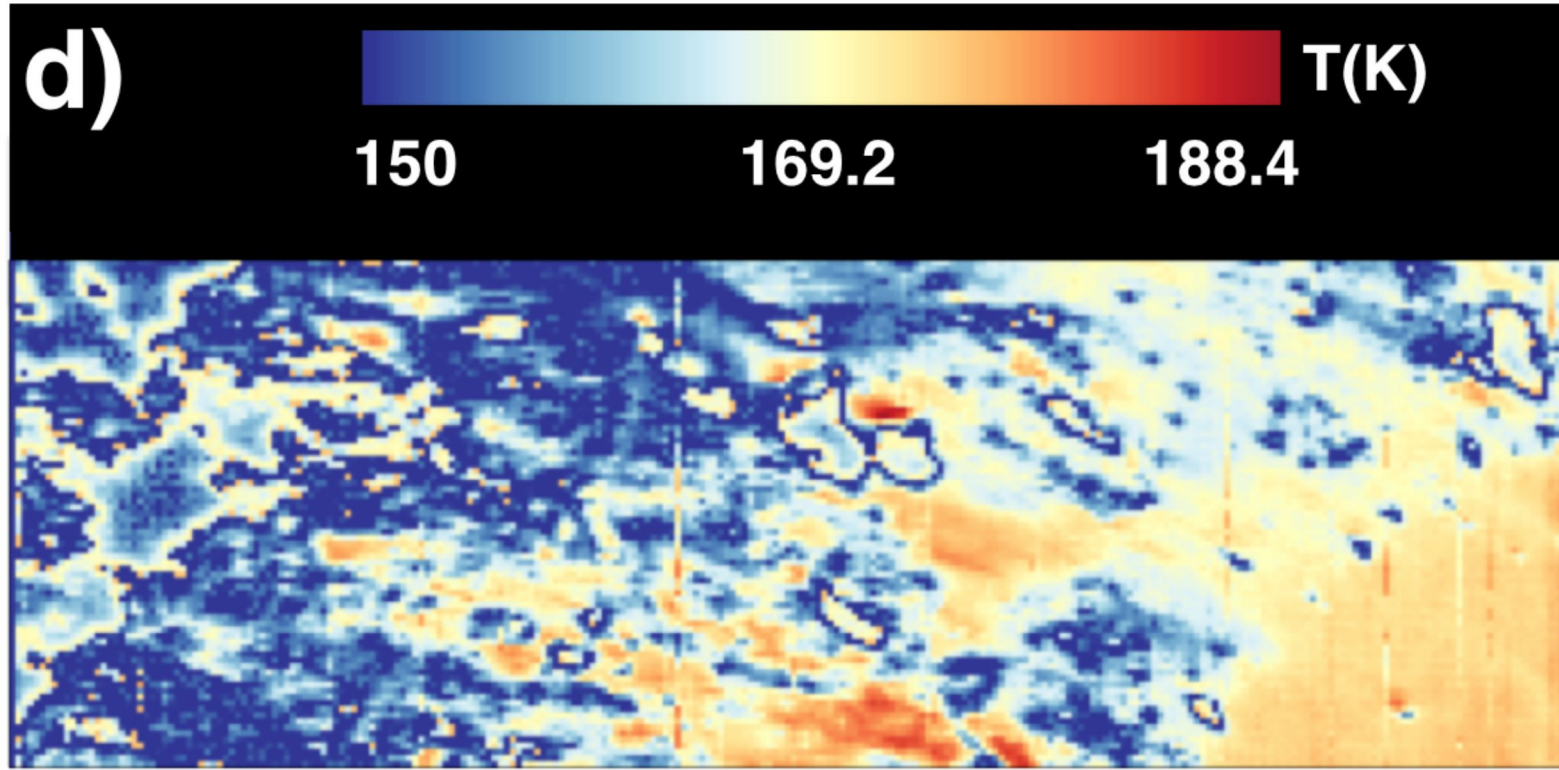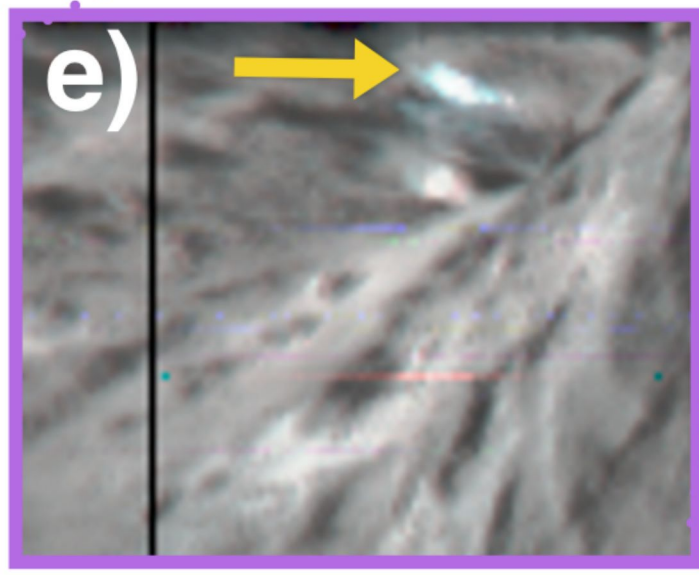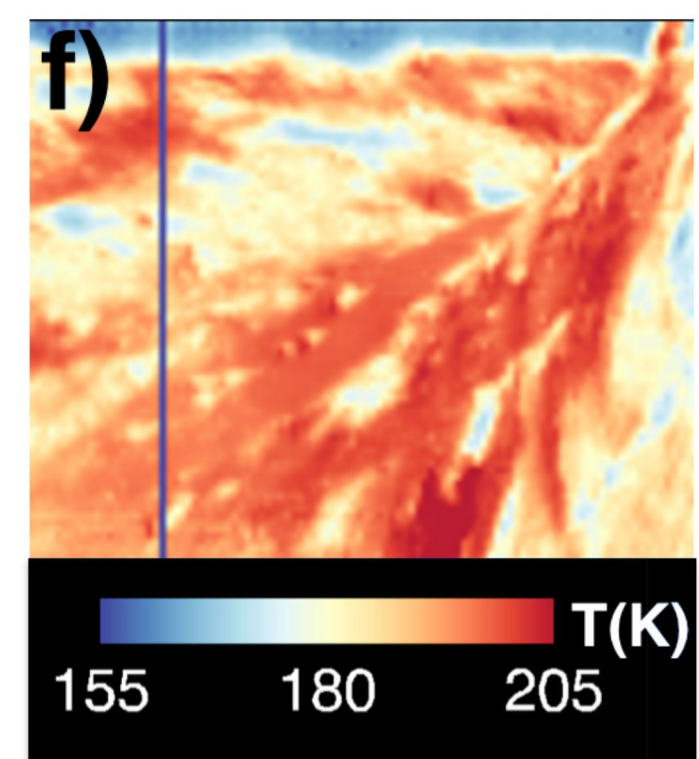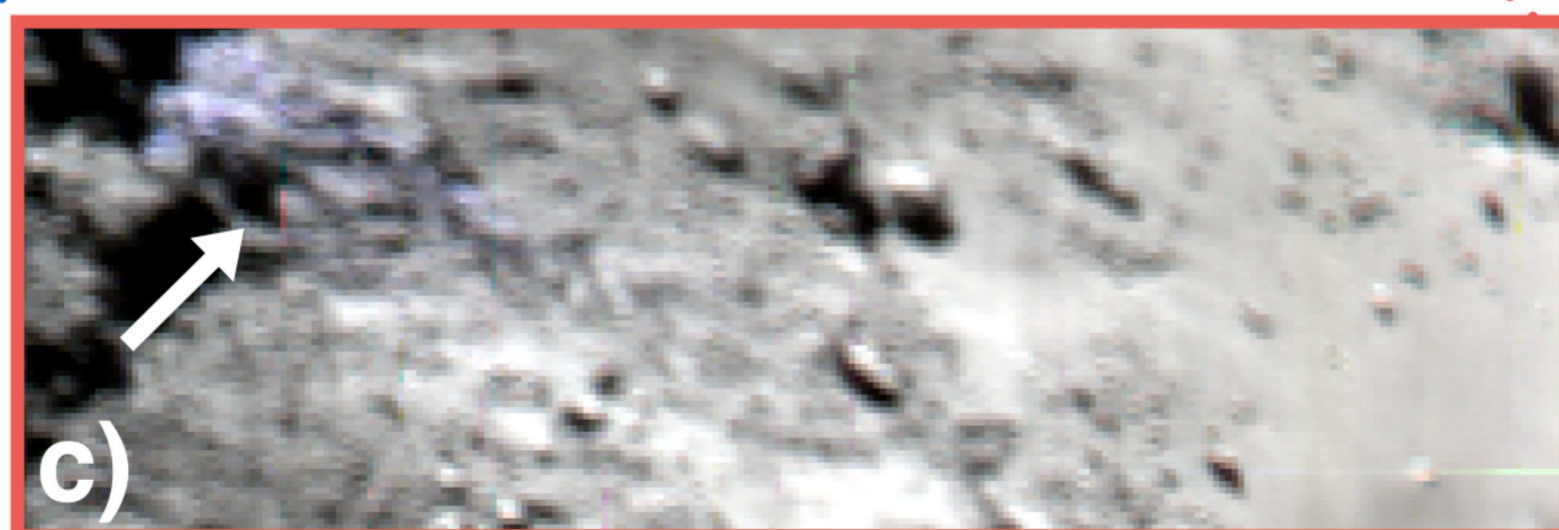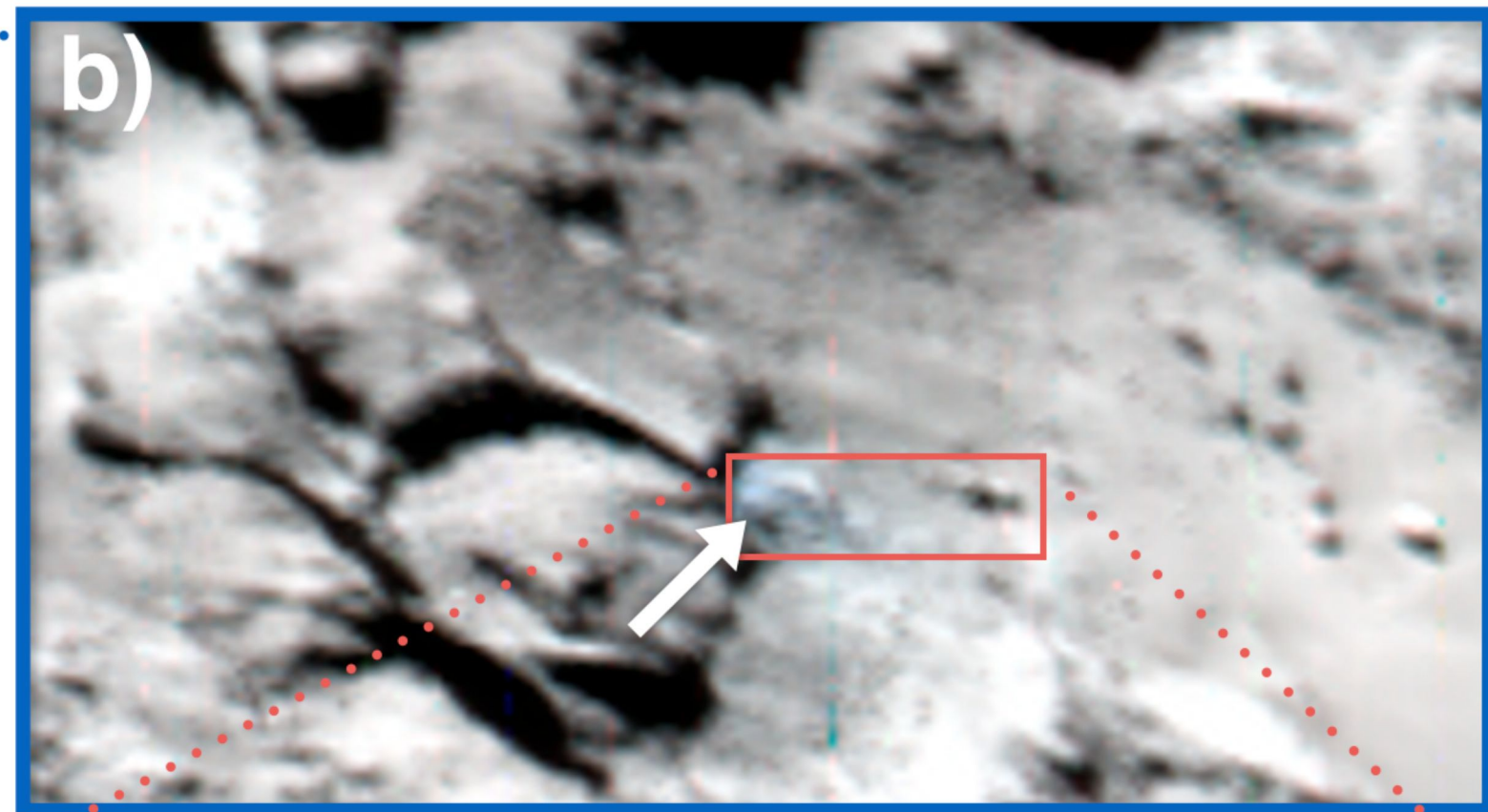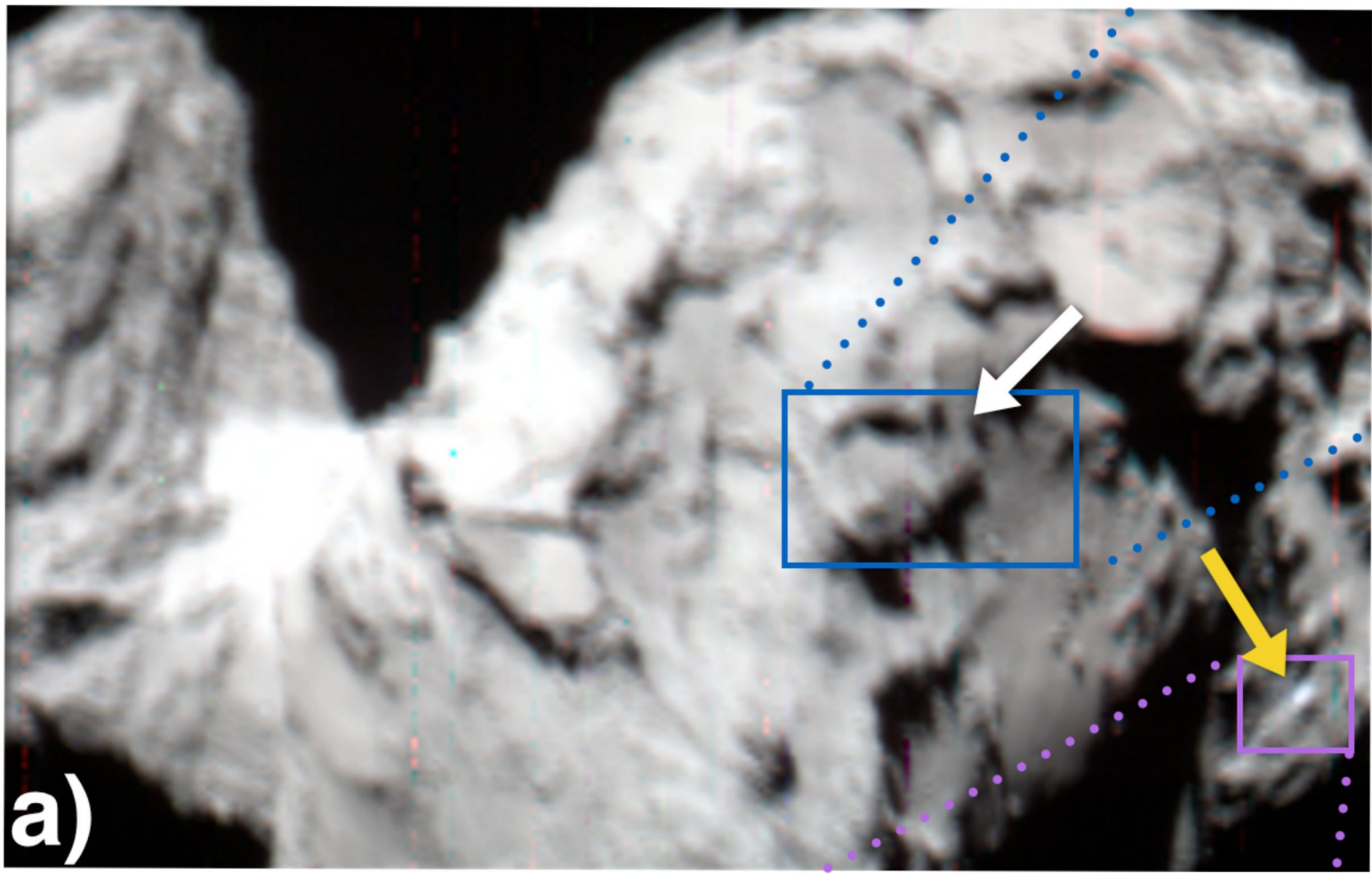
[23] Ammannito, E. et al., On-ground characterization of Rosetta/VIRTIS-M. I. Spectral and geometrical calibrations, Rev. Sci. Instrum.,77, (9), 093109-093109-10, (2006).

[24] Filacchione, G. et al., On-ground characterization of Rosetta/VIRTIS-M. II. Spatial and radiometric calibrations, Rev. Sci. Instrum., 77, 103-106, (2006).

[25] Migliorini, et al., Comparative analysis of airglow emissions in terrestrial planets, observed with VIRTIS-M instruments on board Rosetta and Venus Express, Icarus, 226, 1115-1127, (2013).

[26] A. Raponi, Spectrophotometric analysis of cometary nuclei from in situ observations, PhD Thesis, Università degli studi di Roma Tor Vergata, 131 pages, (2014). Available on arXiv at http://arxiv.org/abs/1503.08172

[27] F. Tosi et al., Thermal measurements of dark and bright surface features on Vesta as derived from Dawn/VIR, Icarus, 240, 36-57 (2014).

[28] F. Tosi et al., Thermal Maps and Properties of Comet 67P as Derived from Rosetta/VIRTIS Data, 46th Lunar and Planetary Science Conference, held March 16-20, 2015 in The Woodlands, Texas. LPI Contribution No. 1832, p. 2156 (2015).

[29] N. Fray, B. Schmitt, Sublimation of ices of astrophysical interest: A bibliographic review, PSS, 57, 2053-2080, (2009).

[30] B. Hapke, Theory of reflectance and emittance spectroscopy. Cambridge University Press. (2012).

[31] M. Ciarniello et al., Hapke modeling of Rhea surface properties through Cassini-VIMS spectra, Icarus, 214, 541-555, (2011).

[32] M. Ciarniello et al., Photometric properties of comet 67P/Churyumov-Gerasimenko from VIRTIS-M onboard Rosetta, Astronomy and Astrophysics, in press.

[33] S. G. Warren, Optical constants of ice from the ultraviolet to the microwave, Appl. Opt. 23, 1206, (1984).

[34] R. M. Mastrapa et al., Optical Constants of Amorphous and Crystalline H_2O-ice: 2.5-22 μm (4000-455 cm^{-1}) Optical Constants of H_2O-ice, Astrophys. J., 701, 1347-1356, (2009).

[35] R. N. Clark et al., The surface composition of Iapetus: Mapping results from Cassini VIMS, Icarus, 218, 831-860, (2012).

[36] L. Dones, J. N. Cuzzi, M. Showalter, Voyager photometry of Saturn's A ring, Icarus, 105, 184-215 (1993).

[37] F. Preusker et al., Shape model, reference system definition, and cartographic mapping standards for comet 67P/Churyumov-Gerasimenko – Stereo-photogrammetric analysis of Rosetta/OSIRIS image data, A&A in press.
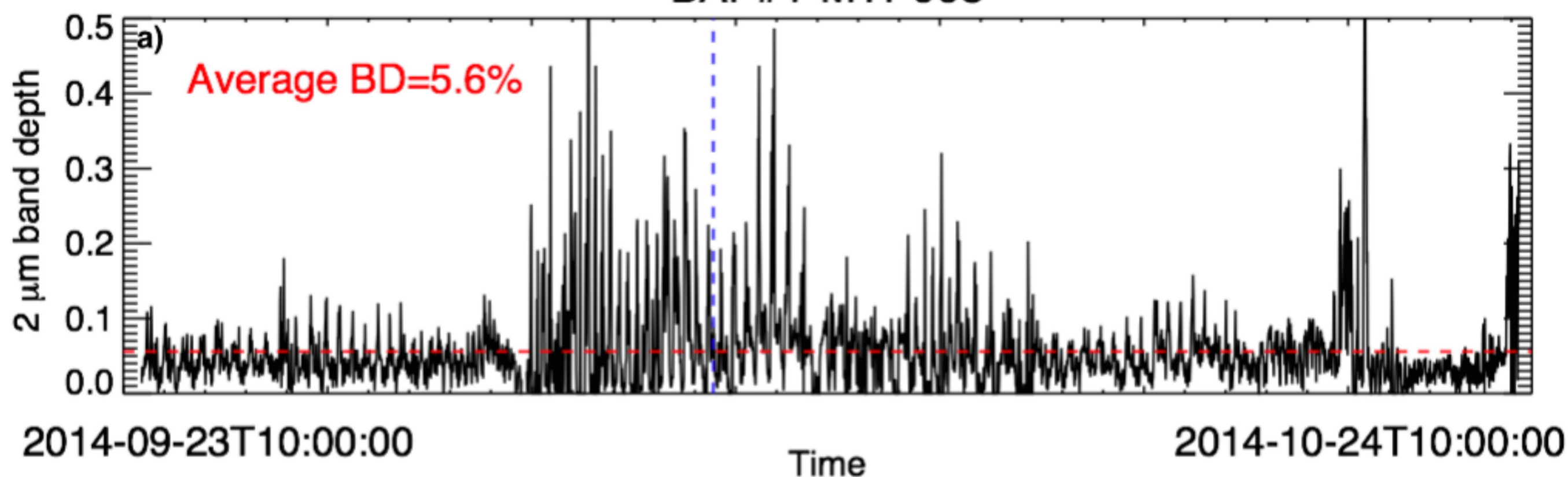
LEGEND FOR EXTENDED MATERIAL FIGURE

Extended Data Figure 1: Water ice grain size distribution derived on the BAP#1. Grains are present in two monodispersed distributions with maxima at 56 μm and at 2 mm corresponding to the intimate and areal mixing classes, respectively. The histogram is computed by selecting only pixels showing a water ice abundance greater than 2% for the intimate and greater than 0.3% for areal mixing.
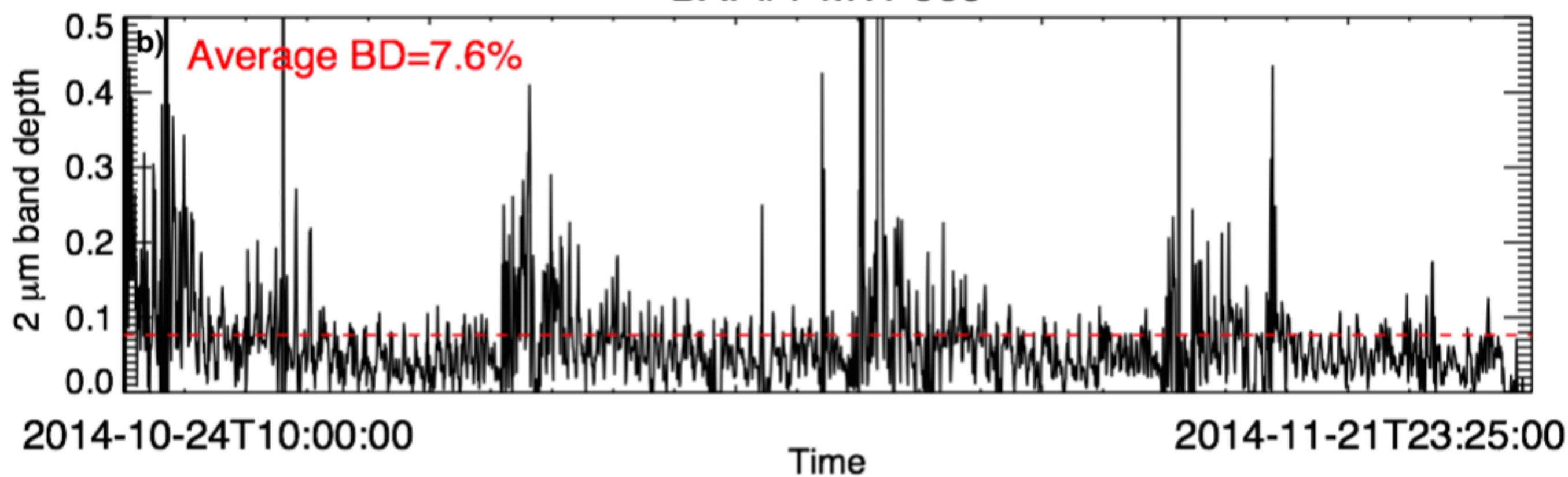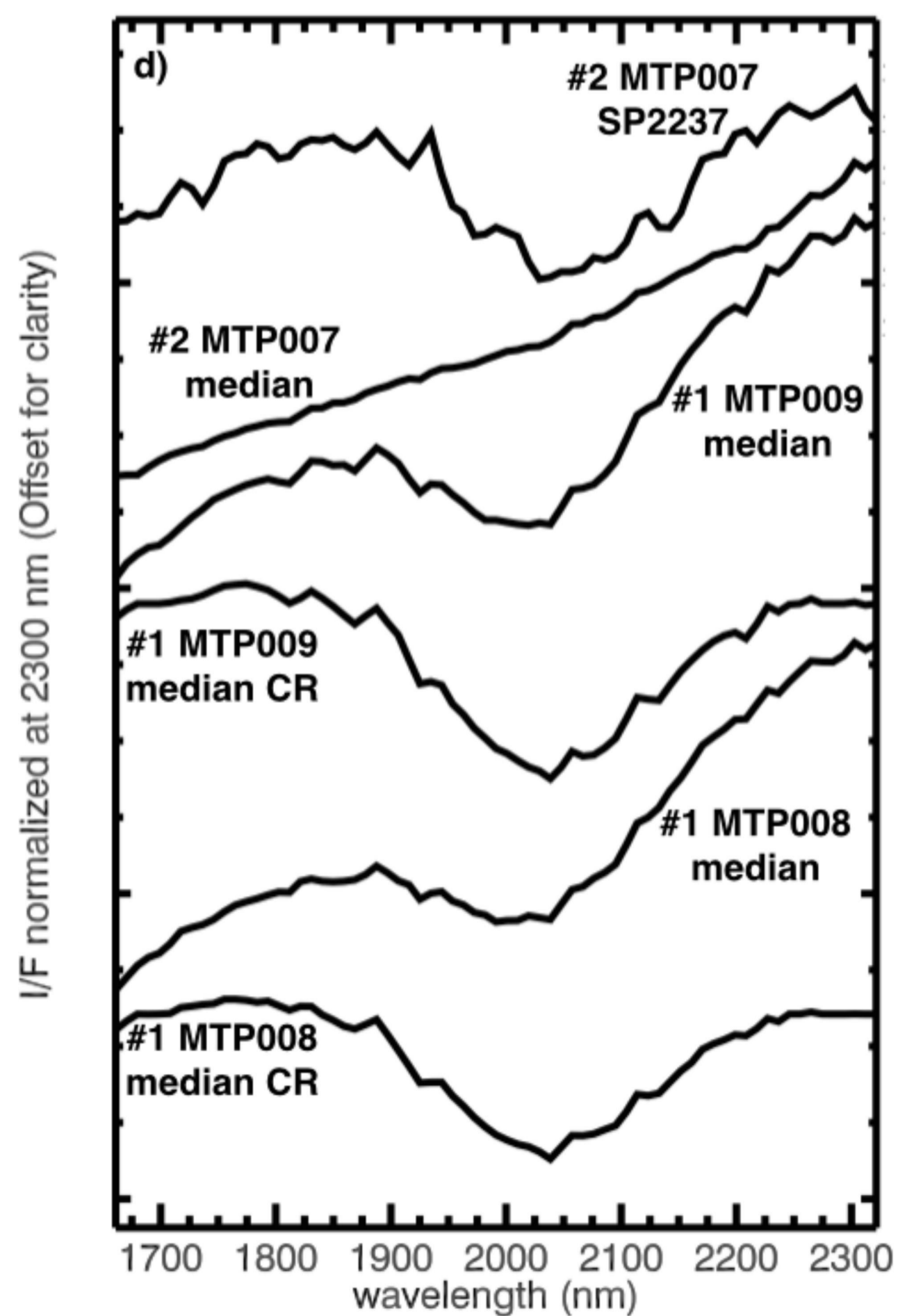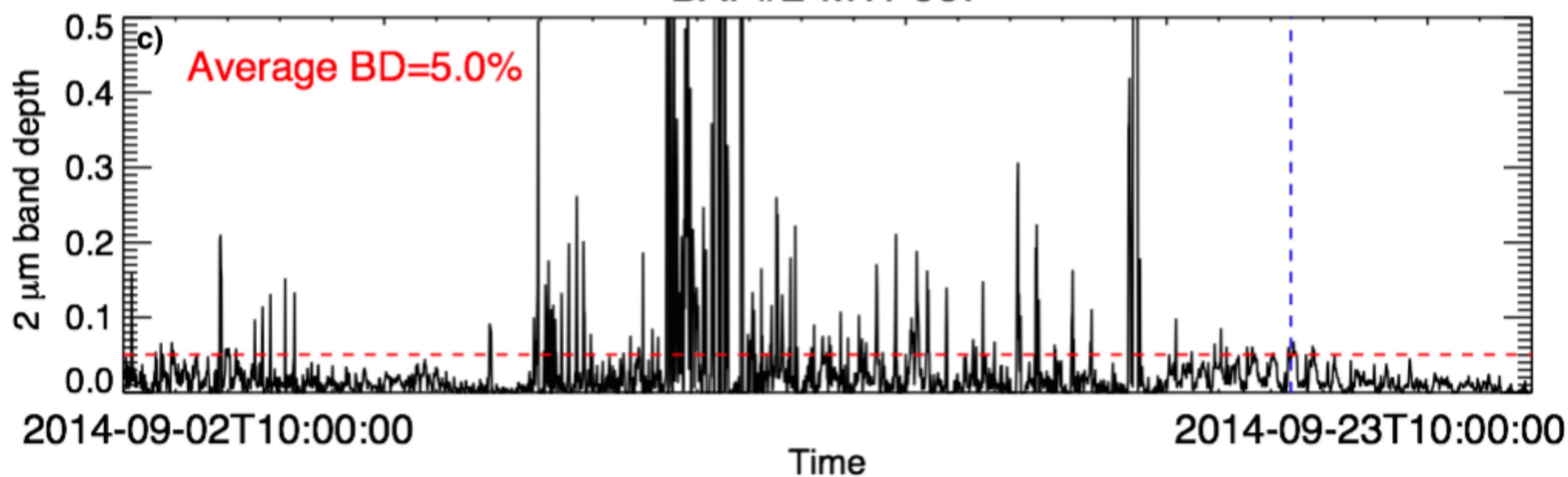
a) b) c) d) e) f)
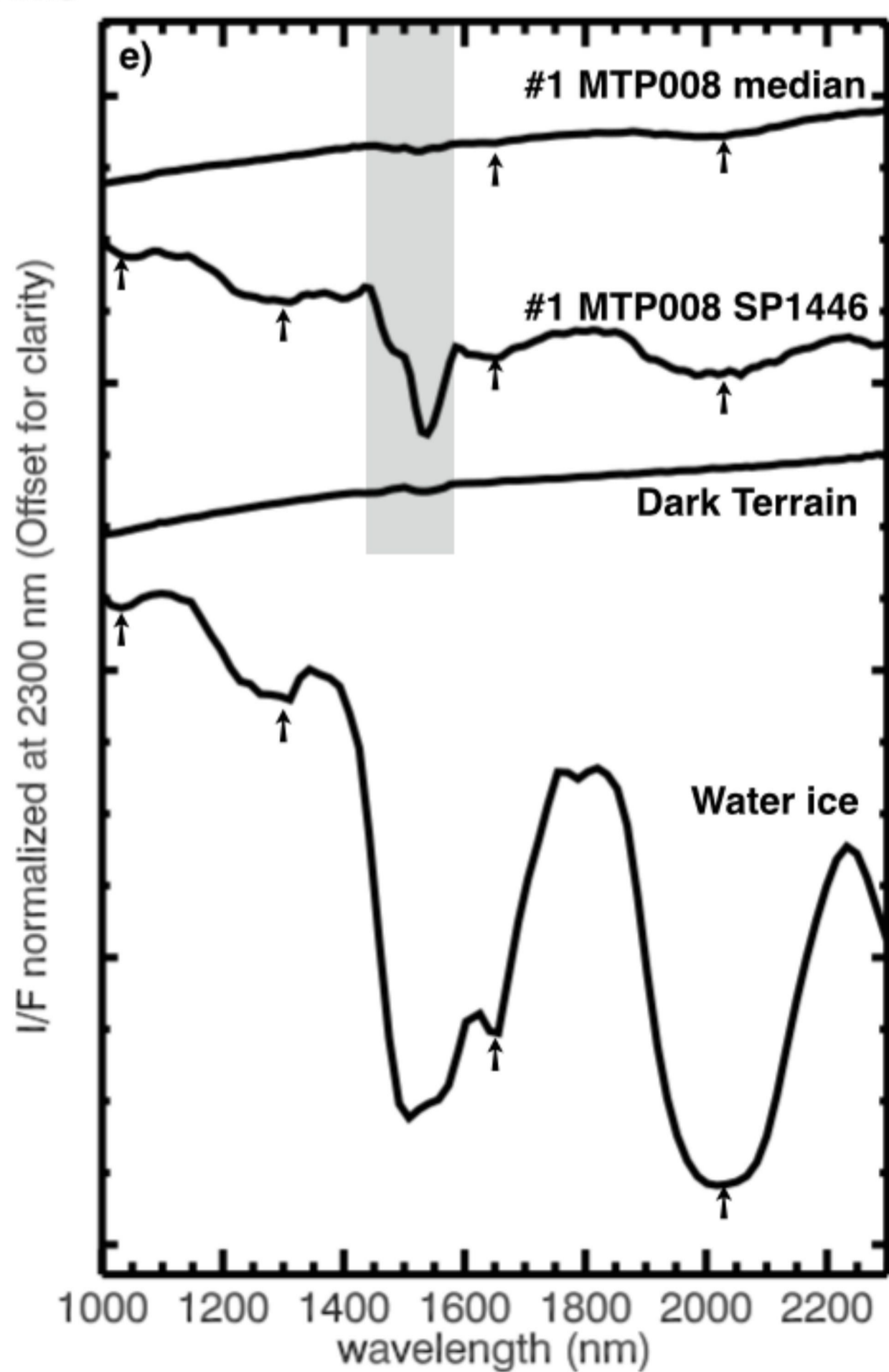
T(K)
150   169.2   188.4

T(K)
155   180   205

BAP#1-MTP008

a) Average BD=5.6%

2 μm band depth

2014-09-23T10:00:00   Time   2014-10-24T10:00:00

BAP#1-MTP009

b) Average BD=7.6%

2 μm band depth

2014-10-24T10:00:00   Time   2014-11-21T23:25:00

BAP#2-MTP007

c) Average BD=5.0%

2 μm band depth

2014-09-02T10:00:00   Time   2014-09-23T10:00:00

d) I/F normalized at 2300 nm (Offset for clarity)

#2 MTP007 SP2237

#2 MTP007 median

#1 MTP009 median

#1 MTP009 median CR

#1 MTP008 median

#1 MTP008 median CR

wavelength (nm)

e) I/F normalized at 2300 nm (Offset for clarity)

#1 MTP008 median

#1 MTP008 SP1446

Dark Terrain

Water ice

wavelength (nm)

a)

observed
modeled

scet = 00371998843
sample = 43
line = 14

Reduced χ^2 = 2.1

intimate mixing
a_{H2O} = 3.4 %
d_{H2O} = 56 µm

areal mixing
a_{H2O} = 1.2 %
d_{H2O} = 1960 µm

b) 50 m

c) 50 m

d) 150 m

e) 150 m

water ice abundance (%)

areal
0.0   0.1   0.2   0.3   0.4   0.5   >0.5

intimate
0.0   0.5   1.0   1.5   2.0   2.5   >2.5

Intimate mix
Water Ice Abundance > 2%

Areal mix
Water Ice Abundance > 0.3%